Check for updates

NANO · MICRO small
www.small-journal.com

MXene and PAN-Based Carbon Fiber Enhanced Bimodal Triboelectric Sensor for Robotic Arm Perception and Control

Fangyang Dong, Qinghe Peng, Guang-An Yu, Hengxu Du, Weilu Sha, Peishuo Li, Yilin Liu, Hu Cai, Taili Du, and Minyi Xu**

Endowing robots with human-like perception and thinking to match the growing intelligentization remains a challenge. Here, an MXene and polyacrylonitrile (PAN) based carbon fiber enhanced bimodal triboelectric sensor (MPBS) is proposed to integrate with a commercial robotic arm, establishing a novel paradigm for perception and control. The touchless and tactile perception performance are further improved by a functional layer doped with MXene nanosheets and electrodes composed of PAN-based carbon fibers. With 2 wt.% MXene, the MPBS electrical output increases by 100%, achieving a touchless sensing range of 200 cm and a peak output ratio of 3.65 V cm $^{-2}$. Integrating MPBSs into flexible fingers, a soft gripper with bimodal perception capabilities is developed. The touchless signals provide valuable insights into material composition, whereas the tactile mode enables precise shape recognition with an accuracy of 99.4%. The further integrated robotic arm utilizes touchless sensing to autonomously explore objects and run control actions when unexpected events occur. 10 types of object materials and shapes are identified with 98.7% accuracy using a convolutional neural network (CNN) that fuses touchless and tactile data. Demonstration of multitask applications, through the AI-enabled robotic arm system, is successfully created for object detection, intelligent sorting, and pipeline inspection.

1. Introduction

Automotive industries, aerospace, and consumer electronics have already implemented programmed robotic arms in their production lines to enhance efficiency and consistency. With the advent of smart manufacturing in Industry 4.0, robots have to face more customized tasks and diversified products.[1] This shift demands the robots to possess enhanced adaptability and flexibility, expanded manipulation capabilities, as well as easier reconfigurability in both hardware and software.[2] Meanwhile, humanoid robots are expected to achieve mass production in the coming years,[3] and before they enter domestic life, robotic technologies will need to address new challenges. Unlike the industry, home spaces are typically unstructured, requiring robots to effectively response and handle unexpected events. These all mean that perception needs to be added to robotic control strategies to sense and manipulate unknown objects or to safely interact with humans. Robotic perception can be categorized based on the perception goals (such as vision, tactility, sound, etc.) or detailed according to different sensor types (such as accelerometers, gyroscopes, temperature and humidity sensors, etc.). Among these perception methods, tactile sense provides robots with information about physical contact, enabling the identification of contact locations, recognition of object shapes, and measurement of contact forces and temperature. Significant and meticulous works have been devoted to advancing tactile sensor techniques, leading to a rapid development in this field.[4] Nevertheless, the robotic tactile perception remains insufficiently mature, and its research and development continue to be challenging, such as insufficient flexibility and limited scalability.[5]

Benefiting from the great advancements in microelectromechanical systems and next-generation information technologies, current research focuses on developing novel flexible tactile skins to cover robotic grippers or hands with tactile sensors, and investigating new methods and algorithms for exploiting tactile information in autonomous manipulation.[2] Up to now, the schemes for realizing tactile perception in soft robots include optical detection,[6] piezoresistive,[7] triboelectric,[8] and electromagnetic effect mechanisms.[9] Mu et al. implanted a micro camera in a transparent silicone-based elastomer to map and measure contact-induced deformation, realizing a high-resolution visuotactile sensing.[6b] Zhang et al. fabricated

F. Dong, Q. Peng, G.-A. Yu, H. Du, W. Sha, P. Li, Y. Liu, H. Cai, T. Du, M. Xu
Dalian Key Lab of Marine Micro/Nano Energy and Self-Powered Systems
Marine Engineering College
Dalian Maritime University
Dalian 116026, China
E-mail: dutaili@dlmu.edu.cn; xuminyi@dlmu.edu.cn

F. Dong, Q. Peng, G.-A. Yu, H. Du, P. Li, Y. Liu, H. Cai, T. Du, M. Xu
State Key Laboratory of Maritime Technology and Safety
Dalian 116026, China

T. Du
Collaborative Innovation Research Institute of Autonomous Ship
Dalian Maritime University
Dalian 116026, China

The ORCID identification number(s) for the author(s) of this article can be found under https://doi.org/10.1002/smll.202503393

DOI: 10.1002/smll.202503393

microstructured triboelectric and piezoresistive layers as an electronic skin, which can perceive dynamic and static pressures simultaneously.[7a] Liu et al. proposed a flexible sensor comprising a magnetoelastic conductive film and a packaged liquid metal coil, that can precisely detect and distinguish touchless and tactile information.[9] Luo et al. designed a fully printed flexible trimodal sensor sheet containing pressure, temperature, and proximity sensing units, with proximity detection activating temperature and pressure perceptions when the event happens.[10] These sensors have been successful in offering multimodal information but often suffer from common structural complexities, are relatively troublesome to fabricate, and involve complicated wiring when integrated into robotic systems. The problems of collaborative optimization for algorithm and hardware are also raised.

Rooted in contact electrification of itself and electrostatic induction with external objects, sensors based on the triboelectric effect have been confirmed to be highly sensitive to touch, pressure, vibration, roll, and slip sensations in the general tactile range.[8] The displacement currents generated by moving charged objects in an electric field and the extremely high signal-to-noise ratio, are much more key for triboelectric sensors to address the major challenges of detecting continuous motion and external stimuli in soft robots.[11] The wide choice of materials that make up flexible triboelectric nanogenerators (TENG) and their high output make them more compatible with soft robots. Meanwhile, the self-generated electrical output in response to the strain and deformation of TENG is more direct, making the subsequent signal processing easier and more interpretable. Jin et al. reported that TENG sensors composed of patterned electrodes and covered dielectric film, by fitting with the soft gripper, can detect sliding, contact position, and gripping mode.[12] Analyzing the big data collected from large-scale array sensors represents a significant research trend. With the aid of the support vector machine, Jin's smart gripper recognized various objects with an enhanced accuracy of 98.1% by increasing sensor channels from 6 to 15. Notably, Lu et al. reported a machine learning-guided design of a flexible tactile TENG sensor system, where output signal parameters, electrode distribution density, and surface microstructures were systematically compared and optimized, enabling a high classification accuracy of 99.58% for tactile perception in six dynamic touch modalities.[13] In contrast, another approach involves simplified designs utilizing functional materials, where a small number of sensors provide sufficient information, complemented by deep learning (DL) techniques to enhance the data interpretation. By leveraging a DL model for data analysis, the soft robotic system proposed by Liu et al. can accurately describe objects based on materials, surface roughness, and shapes, with an accuracy of up to 97%.[9] Additionally, it should be noted that the triboelectric sense has become a popular candidate for multimodal fusion perception due to the widespread electrification, the easy constructability of TENGs, and without preempting of other sensors to make information redundant. However, current research has not yet fully explored the potential of achieving touchless and tactile bimodal perception through flexible triboelectric sensors alone, which would further reduce the difficulty and cost of integration on robots or perception modalities. Moreover, the dexterity level of robots in receiving commands and executing operations through their electronic skin is still greatly inferior to that of humans.[7a] Giving robots sensitive perception and even thinking like human beings is still a focus but also a puzzle in robot research.

In this study, we propose a bimodal self-driven flexible sensor enhanced by functional materials (MPBS) and integrate it with a commercial robotic arm, establishing a soft robotic perception and control paradigm that addresses these challenges, as shown in **Figure 1**. Inspired by the skin structure, the proposed MPBS employs a dual synergistic optimization strategy, doping MXene nanosheets into the functional layer and combining the polyacrylonitrile (PAN) based carbon fiber as the electrode, to significantly enhance both touchless sensing and tactile perception capabilities. First, the interconnected MXene nanosheets improve the charge trapping efficiency. Second, the fully embedded PAN-based carbon fibers with a stacked structure not only expand the effective electrode area within the electrostatic field, thereby increasing the amount of induced charge carriers, but also stabilize charge retention due to the moderate resistivity. The MPBS can actively perceive the object approach and continuous motion via electrostatic induction. Benefiting from both structure and materials, the MPBS demonstrates an ultra-long-distance detection (200 cm) and an outstanding touchless sensing capability (3.65 V·cm·cm^{-2}). To the best of our knowledge, the product of the signal output and the perceiving distance per unit area achieved by MPBS ranks among the highest reported in triboelectric touch-free sensors. By seamlessly integrating MPBSs into artificial soft fingers, we develop a soft gripper with outstanding bimodal perception capabilities for robotic arm end-effectors. The touchless signals enable early recognition of object proximity and provide valuable cues regarding object materials, while the tactile mode delivers precise information on object shapes during contact. Meanwhile, data from the touchless mode allows the robotic arm to autonomously explore objects and run control actions when unexpected events occur. The collaboration between these two modalities not only improves perception accuracy but also facilitates proactive decision making. Furthermore, by training and transferring a convolutional neural network (CNN), we demonstrate an AI-assisted robotic arm system capable of perceiving, describing, and sorting objects based on their materials and shapes. A fully integrated, task-oriented robotic solution from material-, sensor- to system-level intelligent perception and control is presented. This study may advance and expand the robotic interaction with physical world and the interpretability of artificial intelligence in robotics.

2. Results and Discussion

2.1. Construction, Working Principle and Sensing Performance of the MPBS

A schematic view of the MPBS structure is illustrated in **Figure 2a**, which comprises a silicone rubber@MXene nanocomposite as the dielectric layer, and a fully embedded PAN-based carbon fiber felt as the electrode. The actual photograph is shot in Figure 2b. The functional layer-by-layer configuration emulates the multisensory system of mammalian skin, with a simplified skin section and its signal chain presented in Figure 2c. The external epidermis with keratin and hair offers protection, while the internal dermis is rich in tactile corpuscles and nerve endings.

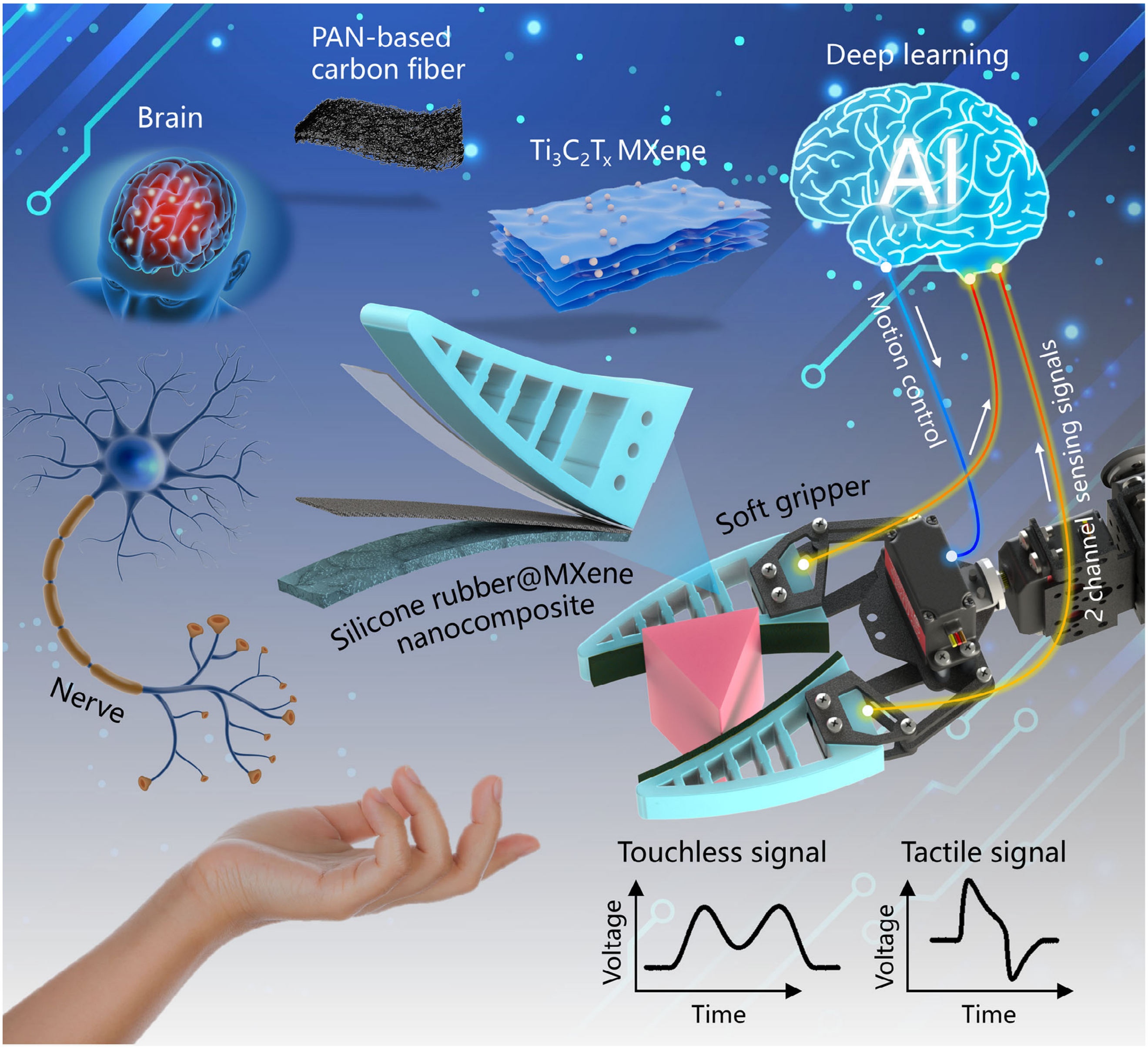

Figure 1. Intelligent robotic arm system via MPBS and CNN for perceiving, describing and classifying objects.

For example, the electroreceptors distributed in the soft dermis layer of the platypus's beak can detect the weak bioelectric signals of prey, and mechanoreceptors can respond to tactile stimuli.[14] Here, the touchless mode of the MPBS mimics the electroreceptors to detect the electrical stimulus based on electrostatic induction. The MPBS can also extract information from the contact deformations, which corresponds to the mechanoreceptors. Additionally, the abundance of collagen and elastin fibers gives the skin elasticity and toughness. Hence, silicone rubber is utilized as a dielectric material base due to its high electronic affinity and flexibility.[15] Furthermore, $Ti_3C_2T_x$ MXene, which features both metallic electrical conductivity and negatively charged surfaces, is employed as a nanofiller to significantly augment the charge capture capability of silicone rubber.[16] The combination of colossal permittivity and intermediate conductivity of the PAN-based carbon fiber improves the electrical output performance in TENG.[17] The experimental Section gives the fabrication process used to prepare the MPBS. It is noting that the surface of the MPBS is demolded on a sandpaper (with 100 meshes per unit area) to create a surface patterned with grooves and protrusions. This not only stabilizes grasping but also enhances the surface electric potential, mimicking human fingerprints and vellus hairs. The monolithic molding of the triboelectric layer with the electrode enables the MPBS to be reliable, preventing the physical detachment of the layered structure during long-term service.

Surface charge density and charge capture capacity mainly determine the output performance of triboelectric materials.[18] Recently, $Ti_3C_2T_x$ MXene, with its metallic core and oxide-/fluorine-based surface terminal groups, has been widely used in triboelectric materials and TENG applications due to high

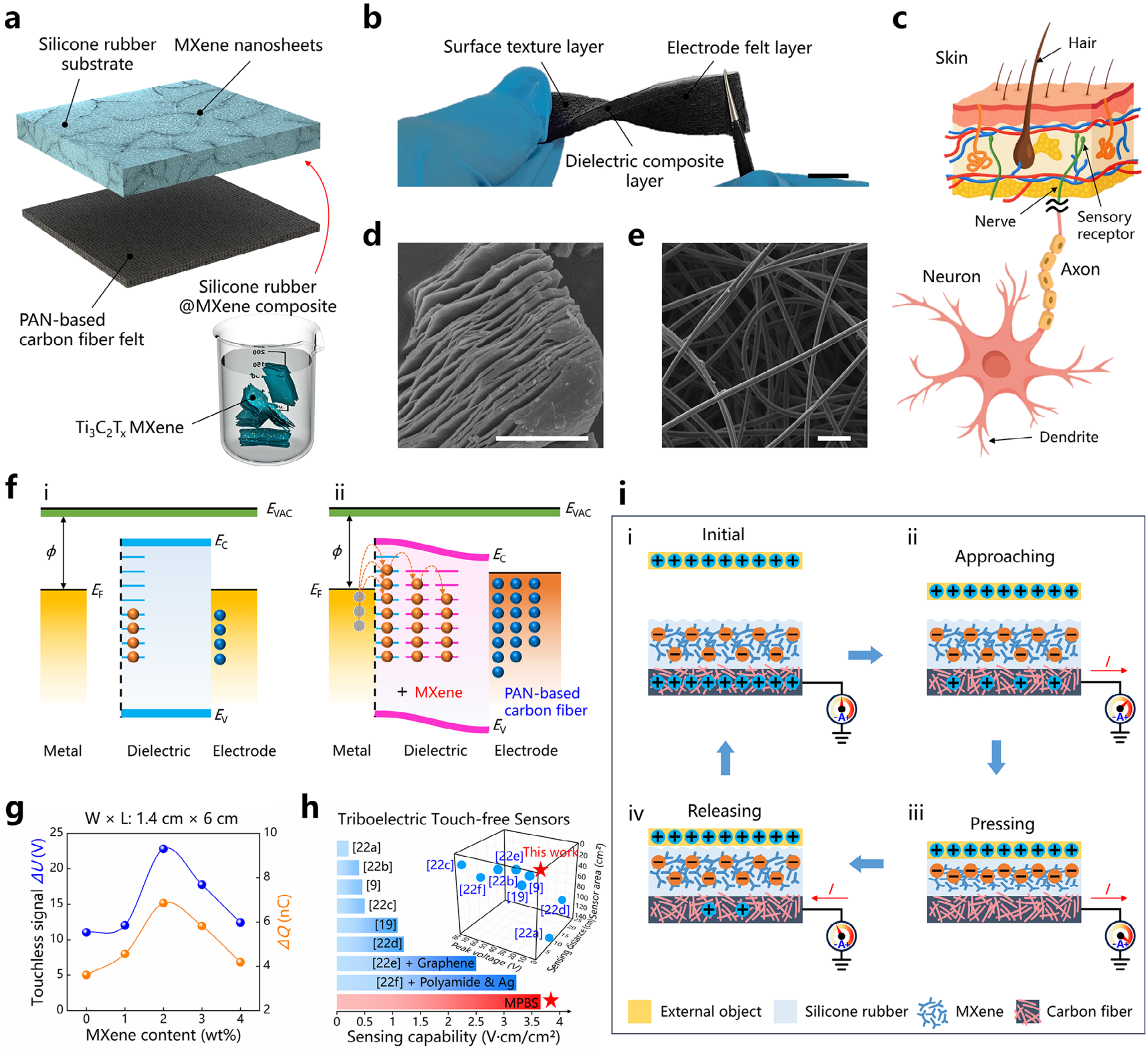

Figure 2. Design and working mechanism of the proposed MPBS. a) Bioinspired structure and b) actual photograph of the MPBS. Scale bar: 1 cm. c) Schematic illustration of the epidermis-dermis-nerve structure of skin. d) FESEM image of the MXene nanosheets. Scale bar: 2 µm. e) FESEM image of the PAN-based carbon fibers. Scale bar: 100 µm. f) Surface states model and the corresponding charge transfer and trapping process. g) Generated V_{OC} and Q_{SC} of the silicone rubber@MXene nanocomposites according to applied MXene content. h) Comparison of the sensing capability with the previously reported triboelectric touch-free sensors. i) Schematic working principle of the MPBS.

electronegativity, good conductivity, and high charge capture capability, significantly boosting the output performance of TENGs.[16] Our previous study has also confirmed that, compared to the pure silicone rubber-based one, the open-circuit voltage (V_{OC}), short-circuit charge (Q_{SC}), and short-circuit current (I_{SC}) are larger for the sensor with silicone rubber@MXene nanocomposites.[19] The high electrical output is attributed to a 2D sheet-like structure with a high aspect ratio of the MXene nanosheets. Figure 2d shows the field emission scanning electron microscopy (FESEM) image of the MXene nanosheets, a distinct layered structure can be seen, which contributes abundantly to boosting the dielectric constant of polymer nanocomposites by inducing microscopic dipoles at the interface between MXene and polymer substrate.[20] The dielectric constant represents the polarizability against an external electric field, which has a proportional relationship with the output performance of TENGs.[16] Moreover, a colossal permittivity is discovered in the PAN-based carbon fiber.[17] Differing from commonly used metallic materials, carbon fibers have the potential to combine high permittivity and moderate resistivity for energy harvesting or conversion.[21] The electrical permittivity is attributed to the material continuity and mobile charge carriers of the PAN-based carbon fiber, which provides a high value of the piezoelectric coupling coefficient, as needed for piezoelectric sensors, actuators, and mechanical energy harvesters. For triboelectric effect, similar to piezoelectric behavior, also operating as electrical energy storage in the form of a dielectric capacitor. Therefore, the PAN-based carbon fiber is integrated as a functional electrode into the MPCS design to leverage its advantage. As shown in Figure 2e, the microstructural order of the PAN-based carbon fibers is relatively lower, with the carbon layers stacking upon each other, causing the conductivity to be not higher.[17] High resistivity reduces output current, while low resistivity reduces output voltage. To further enhance the voltage signal in this study, an intermediate level of electrical resistivity for the electrode is needed.

The mechanism by which the aforementioned functional materials bring an improved performance can be explained by the surface state model of triboelectrification (Figure 2f). After the metal separates from the pure silicone rubber, as depicted in Figure 2f(i), fewer electrons (red dots) remain in the dielectric as the surface states and induce the accumulation of positive charge carriers (blue dots) in the electrode, creating an electric field. When the MXene nanosheets are doped in the silicone rubber, electrons can penetrate and be trapped in the multilayered structure of the MXene within the silicone rubber substrate, as schemed in Figure 2f(ii). They form an enhanced electric field with the abundant mobile charge carriers of the carbon fibers, leading to an increased output. In Figure 2g, the effect of MXene nanosheets' doping weight ratio on the output performance of the MPBS with an active area of 8.4 cm^2 (W × L: 1.4 cm × 6 cm) is investigated quantitatively with a noncontact distance of 5 mm and frequency of 1 Hz. The peak values of both voltage and charge significantly increase to 22.81 V and 6.58 nC as the weight ratio is applied from 0 to 2 wt.%, more than doubling. From the basic equation between V_{OC}, $Q_{SC,}$ and C of $V_{OC} = Q_{SC}/C$, without the external forces, the capacitance between the triboelectric surface and electrode remains constant, thus the voltage is almost directly proportional to the variations in charge. Nevertheless, with further adding the MXene content, the connectivity of the MXene segregated structures increases and the resulting physical contacts create conductive pathways.[16] The accumulated charges in the nanocomposites can be easily released into the air and electrode through the newly generated conductive pathways. The electrical output of the contact mode MPBS at various weight ratios can be found in Figure S1 (Supporting Information), displaying a consistent trend. The results reveal that the rational doping of the MXene nanosheets obviously improves the electrical performance of the MPBS.

Even as separated by 50 mm without contact, the MPBS with an area of only 8.4 cm^2 can generate a peak voltage of more than 6 V, which exceeds the SNC-TENG with a larger area of 32 cm^2 that we previously reported.[19] In this study, the ratio of $V \times d/S$ is proposed to evaluate the touchless sensing capabilities of TENGs, where d and S define the sensing distance and the sensor area respectively, and V is the peak voltage at this moment. As listed in Figure 2h and Table S1 (Supporting Information), the $V \times d/S$ ratio of the MPBS can reach 3.65 V cm cm^{-2}, which is outstanding among previously reported triboelectric touch-free sensors.[9,19,22] Significantly, the external object activities can also be perceived at a distance of 200 cm (see Figure S2, Supporting Information)), indicating the high SNR characteristics and excellent touchless sensing capabilities of the proposed MPBS.

Working on the single electrode mode,[23] the comprehensive touchless and tactile sensing principle of the optimized MPBS is illustrated in Figure 2i. The silicone rubber@MXene and the external object (such as metal) generate equal but opposite charges due to the different electron affinities between two materials. In the initial stage i), the dielectric layer captures the electrons and attracts the positive charge carriers to gather on the electrode for an electric equilibrium. ii) When the external object approaches the MPBS, the built-in electric field of the triboelectric layer changes with the decreasing distance, which leads free electrons to start flowing from the ground to the electrode, generating a current and potential change in the circuit. An electrometer measures and records the electric potential differences. In stage iii), the external object has come into contact with the MPBS and compressed the flexible substrate, and the inflow of electrons continues to reach its limit, meanwhile the potential difference will be its maximum. iv) When the object is released and moves away from the MPBS, free electrons flow back from the electrode to the ground, with a reversed voltage signal. Similarly, if the external object carries negative charges, the electron transfer process between the electrode and the ground will be reversed.

Figure 3a demonstrates the most intuitive touchless and tactile perception of the MPBS through interacting with the experimenter. The MPBS is connected to a sampling and control circuit that manages two LEDs responding to both touchless and tactile signal feedback. Figure 3b and Movie S1 (Supporting Information) record the entire interaction process. When the palm sweeps over the MPBS, the No. 1 white LED on the right lights up while the left LED remains off. The recorded sensory data indicates that the output voltage of the MPBS increases from 0 to ≈6 V, which is signified as a touchless signal since no contact occurs. When the finger presses against the MPBS, the No.2 blue LED illuminates, and the tactile signal surges to ≈25 V. The generation-recovery time of the touchless signal is ≈0.7 s, which is essentially consistent with the duration of the palm sweeping. The response time of the finger pressing tactile signal is less than 0.1 s. The experiment results preliminarily show a high dynamic response of the MPBS, whereas the signal is significantly affected by the actual motion state of the external object.

A measurement system is established to investigate the sensing performance of the MPBS in detail, as schemed in Figure 3c. The MPBS and its insulating support are fixed on a flat plate containing a linear motor. The external object is attached to the actuator (with force feedback) of the linear motor, which enables it to cyclically approach or even press the MPBS while the motor operates. The generated signals are measured by the electrometer, and then transferred to the computer and displayed on the screen. Figure 3d illustrates the touchless signals of the MPBS varying with the distance from the external object. As the distance increases, the output voltage gradually decreases from 31.19 to 6.14 V at the motion frequency of the external object of 1 Hz. In the noncontact range of 0 to 20 mm, the signal attenuation is significant, following a common trend observed in similar studies.[7b,9,19] Uniquely, with the enhancement of the functional materials, the MPBS still possesses strong signal outputs beyond a distance of 25 mm, rather than the failures in many other studies. The inset of Figure 3d can prove the touchless signal remains

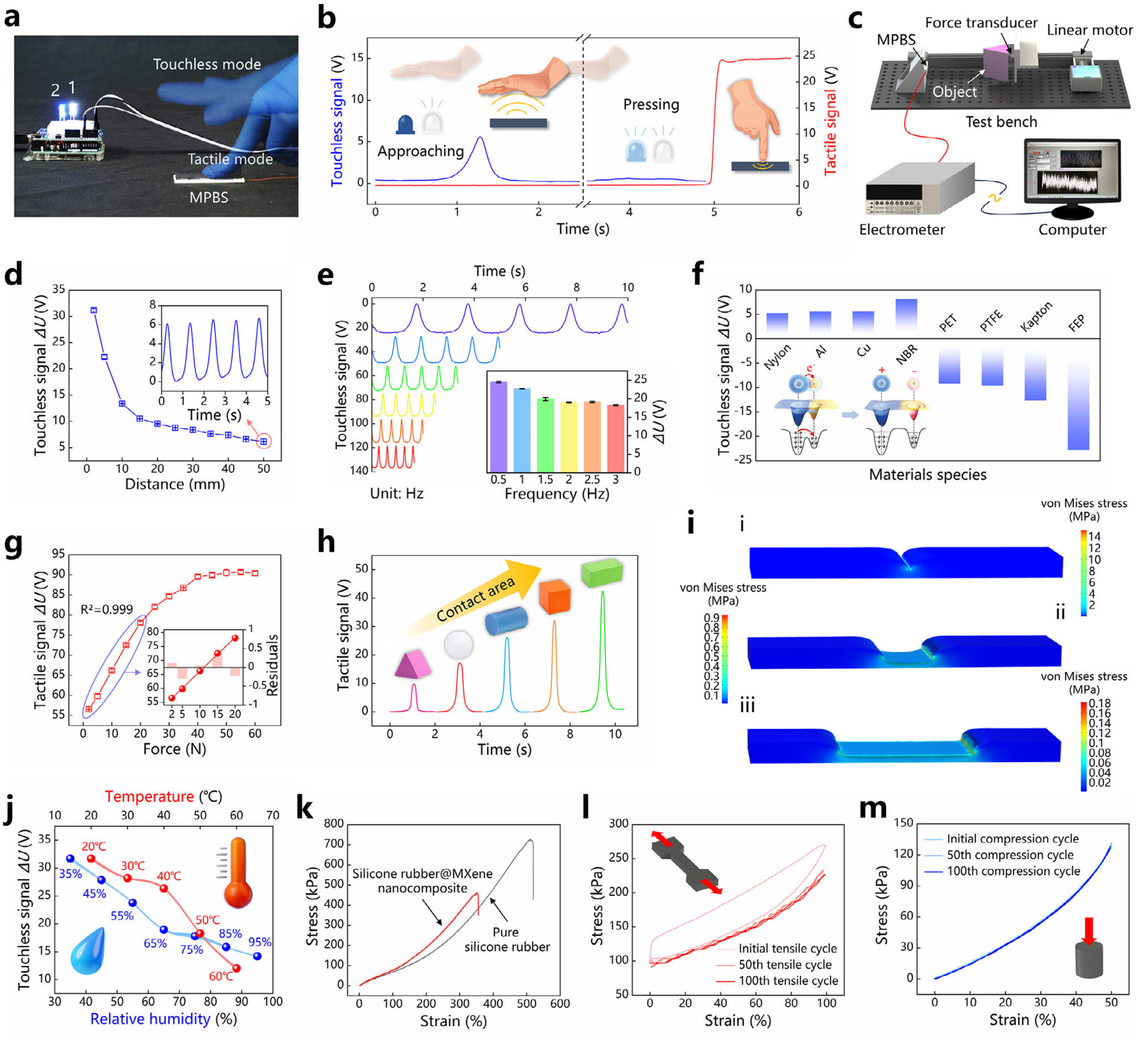

Figure 3. Characterization results of the proposed MPBS prototype for touchless and tactile sensing. a) Photograph and b) bimodal output signals of the MPBS interacting with a human hand. c) Measurement system for the MPBS performance. d) Touchless outputs at various distances between a FEP plate (W × L: 4 cm × 8 cm) and the MPBS. e) Touchless signals at various motion frequencies of the external object. f) Touchless outputs of the MPBS toward different materials. g) Tactile outputs at various vertical contact forces. h) Tactile signals of the MPBS toward different object shapes. i) Finite element analysis results of pressing triangular prism, cylinder and cuboid on the MPBS. j) Touchless outputs at various environment temperatures and relative humidities. k) Stress-strain curves of the silicone rubber@MXene nanocomposite and pure silicone rubber. Stress-strain behaviors of the silicone rubber@MXene nanocomposite under cyclic l) tensile and m) compressive loading.

stable over 6 V even when separated by 50 mm, as mentioned above. The response of the touchless signal to the motion frequency of an external object is further quantified in Figure 3e. With a distance of 5 mm, the touchless signal exhibits a negligible dynamic response time due to the active perception from electric field changes. The voltage amplitude is almost constant across frequencies of 1.5 to 3 Hz, stabilizing above 18 V, and at 3 Hz, the signal can still maintain a complete generation-recovery waveform. Here, 3 Hz represents the cycle time for industrial robots, which needs to be controlled at less than 0.4 s. This rapid dynamic response characteristic enables the MPBS to detect more comprehensive and continuous information, and then broaden its potential applications.

Even more, the objects made of different materials possess varying electron affinities, which will affect their inherent contact electrification and the electrostatic induction with the MPBS. The contact electrification phenomena for the general materials can be explained by an electron cloud/potential model based on the fundamental electron cloud interaction.[24] Their electron clouds overlap due to the physical contact between two materials, transforming the initial single potential well into an asymmetric double well, with an electron transfer occurring (as illustrated in the inset of Figure 3f). After separation, most of the transferred electrons will be kept due to the restored potential barrier. The depth of the potential well in a material determines the ability to attract or repel electrons, thereby dictating the amount and polarity of charges it can carry. The touchless outputs for 8 common laboratory materials at the test distance of 5 mm are shown in Figure 3f. Following the measured triboelectric series,[25] when detecting materials such as nylon, copper foil, aluminum foil, and nitrile, the voltage is manifested as a positive value, while the polymer materials like polyethylene glycol terephthalate (PET), polytetrafluoroethylene (PTFE), Kapton and fluorinated ethylene propylene (FEP) generate negative voltages, with significantly different voltage amplitudes. It is feasible to deduce the types of materials based on the polarity and amplitude feature of the voltage signals obtained from the MPBS.

Moreover, when contact occurs, the MPBS demonstrates the ability to sense pressure. Figure 3g illustrates the relationship between the voltage signal and the vertical contact force applied to the MPBS. The tactile voltage increases with the applied forces ranging from 2 to 50 N. As the force increases from 2 to 20 N, the voltage increases linearly with an R^2 of 0.999. After 25 N, the increase ratio in voltage decelerates, and when the force reaches 50 N, the voltage reaches its plateaus, indicating that the elastic substrate has presumably attained its maximum deformation. Owing to the strain on the entire 3D surface of the elastomer, the MPBS also displays the recognition for spatial shapes, as shown in Figure 3h,i. It is worth noting that in the contact case, the voltage signal of MPBS is affected by both the contact force and area. To decouple the contact information, the vertical contact force between different-shaped external objects and the MPBS is set to 20 N, where the tactile voltage grows with the contact area. When the MPBS is in contact with a triangular prism, a cylinder, and a cuboid respectively, the images of elastomer working are recorded using a camera in Figure S3 (Supporting Information). Correspondingly, the strain and stress distributions on the elastomer are analyzed using finite element analysis, and the results are shown in Figure 3i. When external forces are applied to the MPBS by various objects, the captured tactile images provide a clear visualization of the shape information, while also bringing the varying multidirectional pressure distributions. These results intuitively demonstrate that the MPBS can be used for touchless and tactile bimodal perception.

Considering the service scenarios and environmental changes that the MPBS may encounter during practical applications, the effects of ambient temperature and humidity on the sensor performance are further investigated. A customized experimental setup is designed in Figure S4 (Supporting Information), in which a heating blower and a humidifier are used to control the temperature and relative humidity within a sealed chamber. Figure 3j presents the variations in touchless sensing signals with temperature and relative humidity. As the ambient temperature increases from 20 to 60 °C, the output voltage decreases from 31.71 to 12.03 V at the noncontact distance of 2 mm and the motion frequency of the external object is 1 Hz. This phenomenon is attributed to the escape of trapped charges from shallow layer traps at elevated temperatures,[24] leading to a reduction in V_{OC}. Nevertheless, the MPBS maintains an output voltage above 26 V within the common temperature range of 20 to 40 °C, with a signal attenuation of less than 17%. Similarly, the formation of water layers around the MPBS causes surface charge dissipation, resulting in a gradual decrease in output voltage as the relative humidity increases from 35% to 95% at the controlled room temperature (≈20 °C). Even at a relative humidity of 95%, the V_{OC} of MPBS still exceeds 14 V. These results further verify the charge trapping effect provided by the MXene nanosheets and PAN-based carbon fibers. Collectively, the MPBS exhibits considerable robustness and adaptability under deteriorating environmental conditions.

In practical scenarios, the long-term mechanical reliability of sensor materials is another crucial factor for ensuring a stable sensing performance. To evaluate this, a series of mechanical characterizations on the silicone rubber@MXene nanocomposite are performed using a universal testing machine (Figure S4, Supporting Information). The detailed procedures can be found in the Experimental Section. As shown in Figure 3k, the nanocomposite exhibits a higher stress response under uniaxial tensile loading compared to pure silicone rubber, indicating an increased elastic modulus due to the incorporation of MXene nanosheets. The nanocomposite reaches a fracture strain of 372.11%, while the pure silicone rubber breaks at 537.35%. Although the ultimate strain is slightly reduced, the enhanced stiffness contributes to improved structural robustness, which is desirable for tactile sensor integration. Figure 3l and m illustrate the stress-strain behaviors of the silicone rubber@MXene nanocomposite under cyclic mechanical loading to further assess the durability. The stress-strain curves under cyclic tensile loading (Figure 3l) show that the first cycle exhibits a slightly higher response than the 50th and 100th cycles with a maximum strain of 100%, which nearly overlap, demonstrating a stable mechanical behavior after initial softening. In cyclic compression (Figure 3m), the curves of the 1st, 50th, and 100th cycles almost coincide within a maximum strain of 50%, showing outstanding mechanical stability and resilience. The selected maximum strains (34 mm for tensile and 5 mm for compression) fully meet the practical deformation range required in subsequent grasping. These results collectively confirm that the proposed silicone rubber@MXene nanocomposite possesses reliable mechanical properties and durability under both monotonic and repeated loading, making it highly suitable for long-term deployment in soft sensing applications.

2.2. Shape and Material Identification via CNN Model

Benefiting from its design to emulate soft skin and the plasticity of the silicone rubber substrate, the MPBS can be easily integrated into robots. Grasping is one of the basic skills service robots and industrial manipulators are expected to have. We combined two pieces of MPBS with a deformable robotic soft gripper, as shown in **Figure** 4a, to empower multifunctional object perception and manipulation over both touchless and tactile senses. Through the silicone rubber reshaping, the MPBS is wrapped around the palmar surface of the fin ray effect (FRE) soft finger, as shown in Figure 4b. The FRE fingers are soft and triangular with the crossbeams connecting the front and the back of the fingers. This compliant mechanism allows different parts can

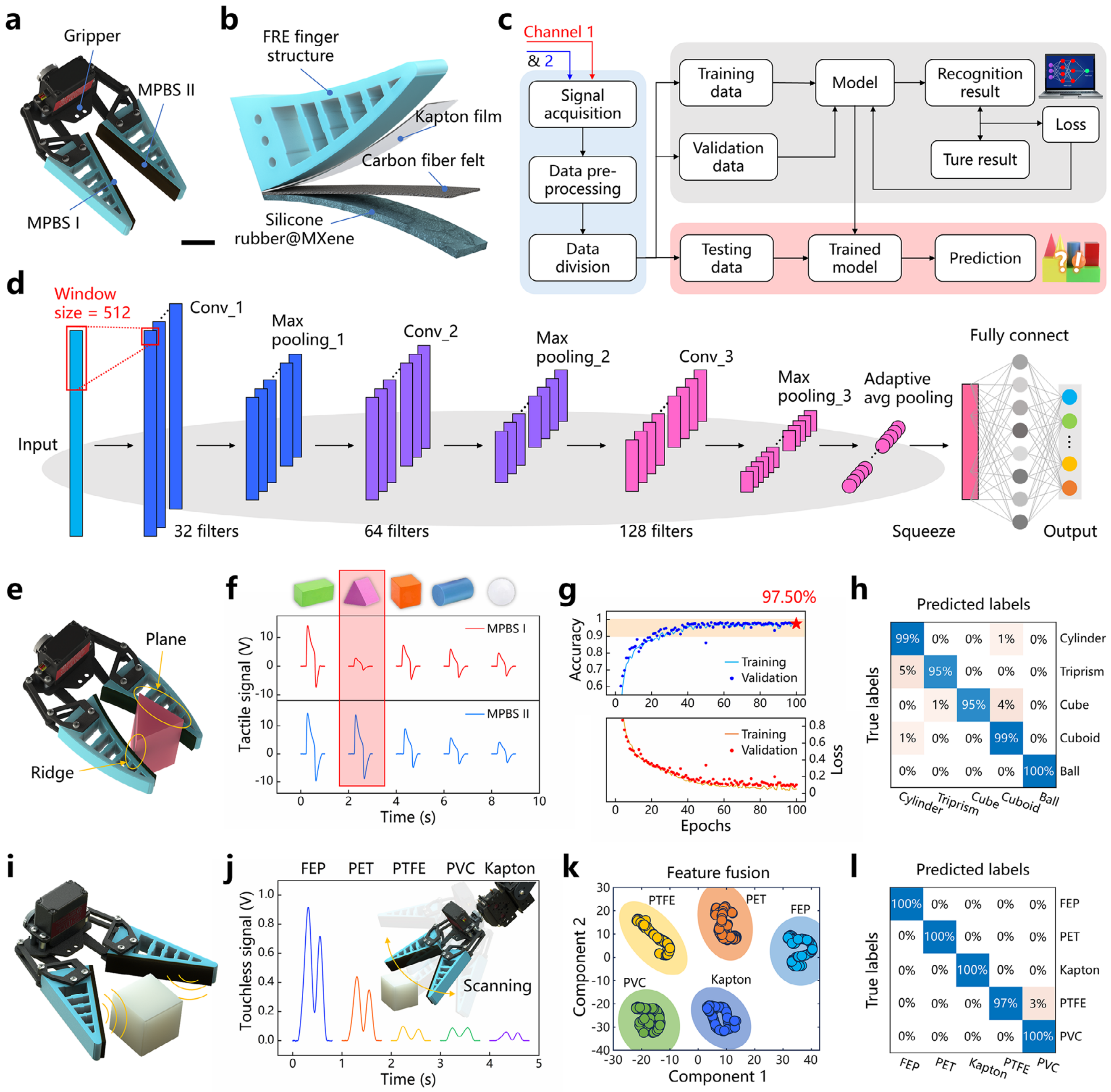

Figure 4. Soft robotic gripper with MPBSs for object recognition. a) Physical depiction of the soft robotic gripper. Scale bar: 2 cm. b) FRE soft finger integrated with the MPBS. c) Schematic flow of DL for object recognition. d) Structure and parameters of the CNN training model. e) Tactile mode of the soft gripper. f) Tactile signals of the gripper correspond to five basic objects (cuboid, triangular prism, cube, cylinder, and ball). g) Training process of the tactile signals for five objects. h) Confusion map for identifying different object shapes. Total accuracy: 97.6%. i) Touchless mode of the soft gripper. j) Touchless signals correspond to five materials (FEP, PET, PTFE, PVC, and Kapton). k) Feature visualization of the touchless signals using the t-SNE analysis. l) Confusion map for identifying different materials. Total accuracy: 99.4%.

bend and deform to conform around objects of various sizes and properties.[26] Significantly, the elastic modulus of the FRE finger structure is higher than that of the MPBS, by their double deformation, both of which will provide more information for tactile sensory.

In robot hand applications, tactile signals are used to recognize objects as one of their main tasks. The recent technology fusion of AI and integrated circuits has driven great advances to form an intelligent system in those technologies related to the process of data acquisition, processing/analysis, and transmission.[27] To extract the full sensory information from sensors, DL-assisted data analytics can be applied to the sensory dataset to realize the object recognition intent.[28] CNN, a promising representative DL technique for automatically extracting features from signals by its convolutional layers, has been proven to be effective for analyzing triboelectric datasets.[29] In particular, the CNN model is effective in learning spatial and temporal correlations between multiple input channels, making it well-suited for fusing the dual-channel signals acquired from two fingers for robust object perception. The object recognition flowchart under the DL architecture introduced in the MPBS-based robotic soft gripper is displayed in Figure 4c. The generated raw voltage data in the time domain of 2 channels from two soft fingers is acquired by an Arduino Uno R3 microcontroller, with a baud rate of 9600 bps, and recorded using the corresponding object labels. After preprocessing the data collected from known objects, it is divided into training set, validation set, and test set in the ratio of 7:2:1. Then, the training set and validation set are combined with the CNN model for continuous training and iteration. As the amount of training data increases, the model gradually approaches the actual target. Finally, the model performance is evaluated by the test data not seen in training. The proposed network architecture of the MPBS object recognition (Figure 4d) consists of three convolutional layers, three max-pooling layers, one adaptive average pooling layer, and one fully connected layer to predict the recognition results of five labels. The detailed parameters used to construct the CNN model are listed in Table S2 (Supporting Information).

Figure 4e,f illustrate the utilization of CNN to recognize five basic 3D objects: cuboid, triangular prism, cube, cylinder, and ball. In the process, the voltage data of five objects with different shapes is collected by repeating the gripping and releasing actions under a fixed gripping force of 20 N. The detailed 2-channel signals from two MPBSs for five objects are visualized in Figure 4f and the data length for each channel is 500. The triboelectric waveform samples of five types present their own distinctive featured patterns, including important features such as amplitude, slope, duration, and interval of peaks, which helps in the feature selection of CNN model.[30] For instance, as depicted in Figure 3h, the magnitude of the contact area gives the distinguishable amplitudes. While the signals from similar or symmetrical surfaces tend to be consistent, demonstrating the grasping stability and the perception robustness of the MPBS. It is worth noting here that when the triangular prism is grasped (Figure 4e), the triboelectric tactile signal for the ridge in Channel 1 has extremely low amplitude information, even though the signal corresponding to the plane of the triangular prism (as Channel 2 in the red shadow of Figure 4f) is similar to that of the cuboid. Each object is gripped 100 times to ensure dataset reliability and sample diversity. The length of the sliding window is determined to be 512 to ensure that each sample can cover complete information. The training process of the CNN model is visualized in Figure 4g, where the accuracy of both the training set and validation set rapidly increases with the training epochs. After 40 epochs, the accuracy of both reaches more than 90%, and the oscillation amplitude of accuracy curves has reduced to less than 10%. The accuracy and loss curves tend to be horizontal after 40 epochs, indicating that the model has converged, and the validation set reaches a maximum accuracy of 97.5%. Figure 4h shows the confusion matrix of the five labels classification using the test set. The trained model has a high positive predictive value and true positive rate for object shape recognition, with an average accuracy of 97.6%, and it has generalized enough to avoid overfitting.

Originating from the contact electrification between different materials, TENGs are particularly sensitive to the type of materials. Thus, triboelectric sensors have made significant progress in material recognition applications.[31] And yet, the contact-generated output signals are still disturbed by other factors, such as varying contact forces, whose coupling to the material polarity poses a challenge to the stability and precision of signals. This complexity hinders the direct deployment of triboelectric sensors in practical applications, especially when faced with real objects with multiple properties, including but not limited to shape and material, the recognition ability of sensors is put to the test. Nevertheless, as shown in Figure 3f, the touchless voltage of MPBS exhibits specificity to the material series. Here, we try to recognize objects of different materials using touchless signals to decouple pressure and material information. In Figure 4i, the servo motor on the wrist controls the robotic gripper to scan the measured object in a noncontact manner. In the process, the gripper remains open with both MPBSs facing the object and sweeping from its bottom to the top. The actual demonstration can be found in Movie S2 (Supporting Information). Figure 4j displays the MPBS output signals for sensing five materials of FEP, PET, PTFE, PVC, and Kapton. To capture more feature information, each signal sample contains two consecutive scanning processes, as shown in the inset of Figure 4j. Limited by the maximum baud rate, the waveform sampling is not as exquisite as shown in Figure 3. The 50 signal samples of each material are acquired for the CNN training. Intuitively, the penultimate layer of the model is visualized using the t-distributed Stochastic Neighbor Embedding (t-SNE) algorithm in Figure 4k. All test samples present a good clustering effect, with the points in the same color closely grouped together and hold a clear boundary with other classes, indicating that the model can fully exploit the abstract features of different labels. The confusion matrix of the five-label classification is given in Figure 4l. Agreeing with the clustering results, a remarkable material identification accuracy of 99.4% is obtained. All samples with obvious feature differences are detected, where the touchless mode triboelectric sensors demonstrate the potential to facilitate material sensing. Object recognition is an important element in human-robot interaction and autonomous manipulation.[32] Combining touchless and tactile dual-modal sensory information from the MPBSs to explore and recognize an object offers a considerable opportunity for robots.

2.3. Touchless Control Method for Robotic Arm

Before performing a grasping procedure, the robot must plan to grasp. Humans often perform tactile servo actions almost subconsciously, for example, when they search for a key in the pocket.[2] In cases without visual information, the motor response is coupled with the tactile feedback only. In the robotics literature, the tactile feedback is mainly used for an event drive,[33] has been rarely employed inside a control loop because of the noisy signals coming from tactile sensors.[34] By the touchless sensing, the robot can detect the presence of object beforehand, without relying on the contact event trigger or the visual system confirmation.[10] The MPBS-based robot soft gripper is integrated with a rigid robotic arm serving as an end-effector, as shown in **Figure 5a**. The perception and control system diagram

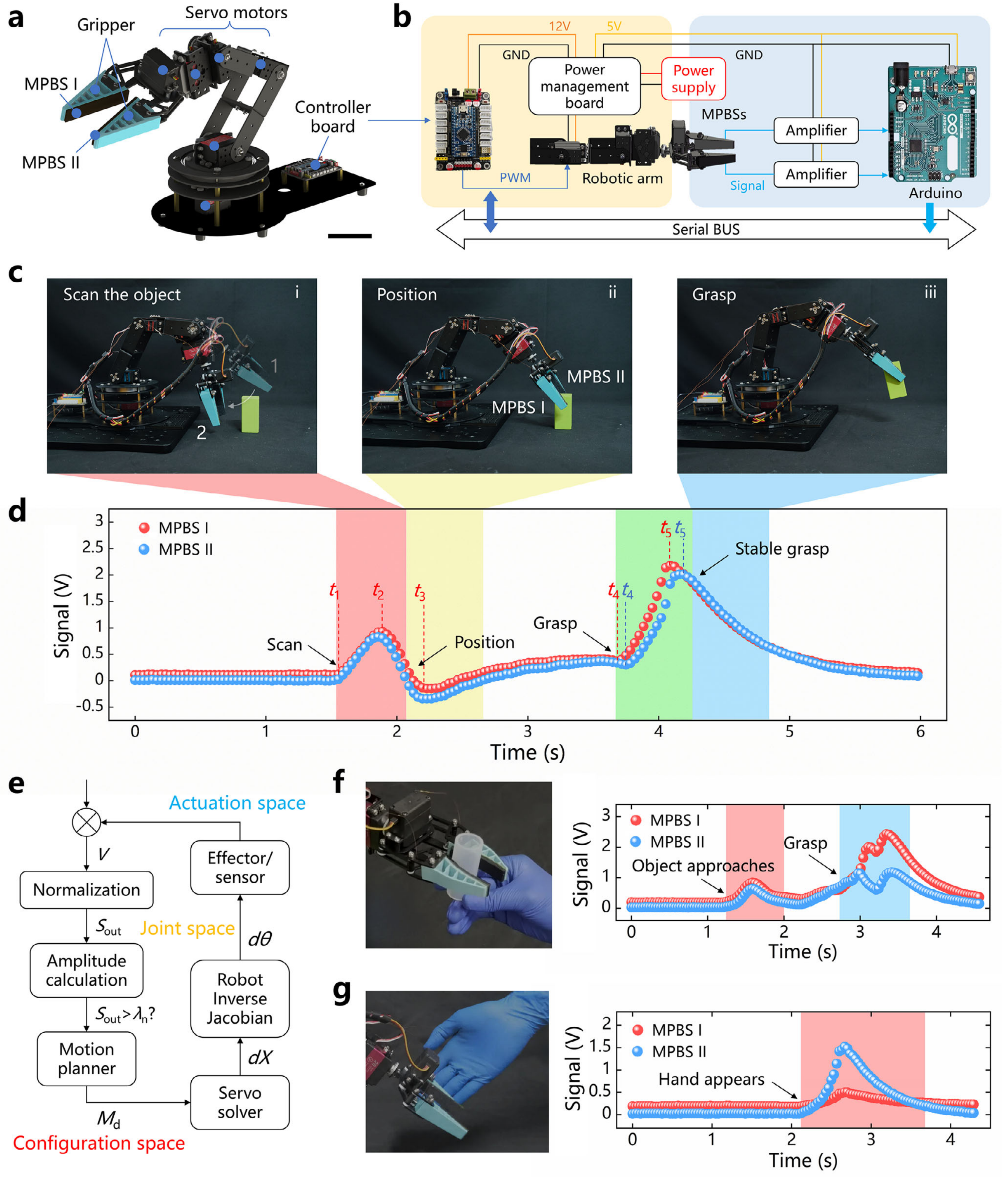

Figure 5. Touchless kinematics control method for the robotic arm equipped with MPBSs. a) Physical depiction of the robotic arm. Scale bar: 5 cm. b) System-level block schematic of the triboelectric bimodal perception and control system for robotic arms. c) Demonstration and d) corresponding output signals of the robotic arm with MPBSs scanning, positioning and grasping the object. e) Closed-loop control framework based on triboelectric signals. f) Active grasping and g) emergency stop in response to an approaching object or human hand.

of the integrated robotic arm is illustrated in Figure 5b. The 2-channel signals from MPBSs are acquired using Arduino, and then transmitted to the computer via serial communication. The controller board connected to the computer outputs the robotic arm joint angles, which are used by 6 joint servo motors to drive the end-effector to a defined position in the 3D task space for performing the exploration and grasping. In a typical operation, 30° rotation of servo motor, the response time of the proposed system architecture is ≈104 ms. The detailed calculation process can be found in Note S1 (Supporting Information). A successful grasping task performed by the constructed robotic arm system is displayed in Figure 5c, and the bimodal signals are recorded throughout the entire interaction in Figure 5d. The continuous camcording is demonstrated in Movie S2 (Supporting Information), where the process can be divided into four steps. In step (i), the gripper with the MPBSs scans contactlessly from Position 1 to 2, and generates touchless signals from two channels. As shown in Figure 5d, the triboelectric signal appears two almost overlapping peaks from the time t_1. By encoding 6 motion commands, the robotic arm segment deforms accordingly to send the end-effector to the designated position when touchless signals of MPBSs reach a predetermined threshold. Figure 5e lists the basic servo control architecture of the robotic arm system, where V represents the measured voltage of the MPBS, S_{out} is the normalized voltage signal, and λ_{n} is the trigger threshold value. The motion planner defines the action sequences, M_{d}. The servo solver translates the changes in actions to the position of the end-effector dX. Then, the Robot Inverse Jacobian is applied to calculate the robotic arm joint values $d\theta$ from the end-effector position in the Cartesian space. As step (ii), when $S_{\mathrm{out}} > \lambda_1$, the gripper is adjusted to the median position of the scanning stroke, which corresponds to the peak value at t_2, to realize the positioning of the object. And the triboelectric signal is returned to 0. It is worth noticing that the amplitudes and phases of the three feature points t_1, t_2, and t_3 remain the same in the first two steps (where Figure 5d down-samples to 1/10 of the raw data), which verifies the synchronized response of two MPBSs. Later, the gripper closes in step (iii) and the triboelectric signal suddenly increases, indicating that the contact with the object has occurred at the moment t_4. The time lag arising in the period from t_4 to t_5 is due to the MPBS I being the first one to touch the measured object. After t_5, the object is stably gripped and lifted in step (iv), the 2-channel signals return to synchronization, and the robotic arm grasping procedure finishes.

Furthermore, we have also extended the robotic arm with adding active grasping and emergency stop functions that utilize touchless control (as demonstrated in Figure 5f,g and Movie S3 and S4 (Supporting Information)). These functions increase the flexibility and safety of the robotic arm in carrying out various tasks. As the object approaches the gripper, illustrated in Figure 5f, the touchless signal begins to rise, and once the threshold λ_1 is exceeded, the robotic arm probes forward to grasp the target. The signal change in the red shadow is caused by the handheld object sliding. In Figure 5g, the human hand suddenly approaches the running robotic arm, the signal steeply breaks through the higher threshold λ_2, and the robotic arm immediately stops to prevent an accidental collision. In this case, the channel signal of the MPBS II is more outstanding because of its proximity to the human hand. These experimental scenarios show that the robotic arm integrated with the MPBS can detect its surroundings and react appropriately. Therefore, the MPBS has the potential to be further developed into an electronic skin for robotic arms, providing comprehensive anti-collision protection for human-robot interaction and multi-robot collaboration, ensuring the security of both personnel and equipment.

2.4. Multitask Demonstration with Intelligent Robotic Arm System

To explore the potential of using the bimodal perception and control system in future practical applications, a series of camera-free service scenarios around the integrated robotic arm are constructed. Leveraging the noncontact scanning function investigated above, a robotic arm patrolling task is planned with different objects and placements for testing, as shown in **Figure 6**a,b. The route of the robotic arm is divided into five areas with some objects scattered in individual ones, and the gripper scans through them in sequence to look for the objects. Basing the threshold judgment, we developed a real-time object detection system using Python, where the states of objects are binary (present or absent) in each area. As the computer-controlled robotic arm drives the gripper to scan these objects (Figure 6a), the signal peaks from the dual channels are rendered in real-time on the screen, and the system determines and suggests that an object is present in the current area. Figure 6b illustrates that the output signals from two MPBSs remain stable without any obvious fluctuations, during patrolling in clean areas. Movie S5 (Supporting Information) records the successive scanning process across five areas with real-time triboelectric signals.

On the basis of the patrolling task, the CNN model is further introduced into our robotic arm task to capture various physical features of objects, developing an intelligent sorting system. Mixed information from 10 objects featuring variations in materials (FEP, PET, Kapton, PTFE, and PVC) and shapes (cylinder, triangular prism, cube, cuboid, and ball) is generated and collected, as shown in Figure 6c. The acquired signals, which underwent a series of preprocessing, are fed to the CNN model constructed in Figure 4d for training. Figure S5 (Supporting Information) presents the training process and the feature visualization results. The training and validation curves exhibit good convergence without any signs of typical overfitting. Additionally, the t-SNE visualization of the output features reveals a good distribution in the feature space with clearly class boundaries, further confirming the strong separability of the extracted features. Figure 6d shows the confusion matrix for ten-label classification, of which the average recognition rate reaches 98.7%, highlighting the applicability of the model in distinguishing different object features. The trained model is transferred to the robotic arm system to perceive, describe and sort the objects in real time, while the robotic arm picks and delivers the targets depending on the identified results. The procedure of intelligent sorting has been predefined by the experimenter, which includes object finding, touchless material recognition, grasping, tactile shape recognition, and final delivery. The category notes of 'Cuboid', 'Cylinder', and 'Ball' are labeled on the baskets respectively for the final delivery. The complete process can be found in Movie S6 (Supporting Information). In Figure 6e,i) the gripper performs a

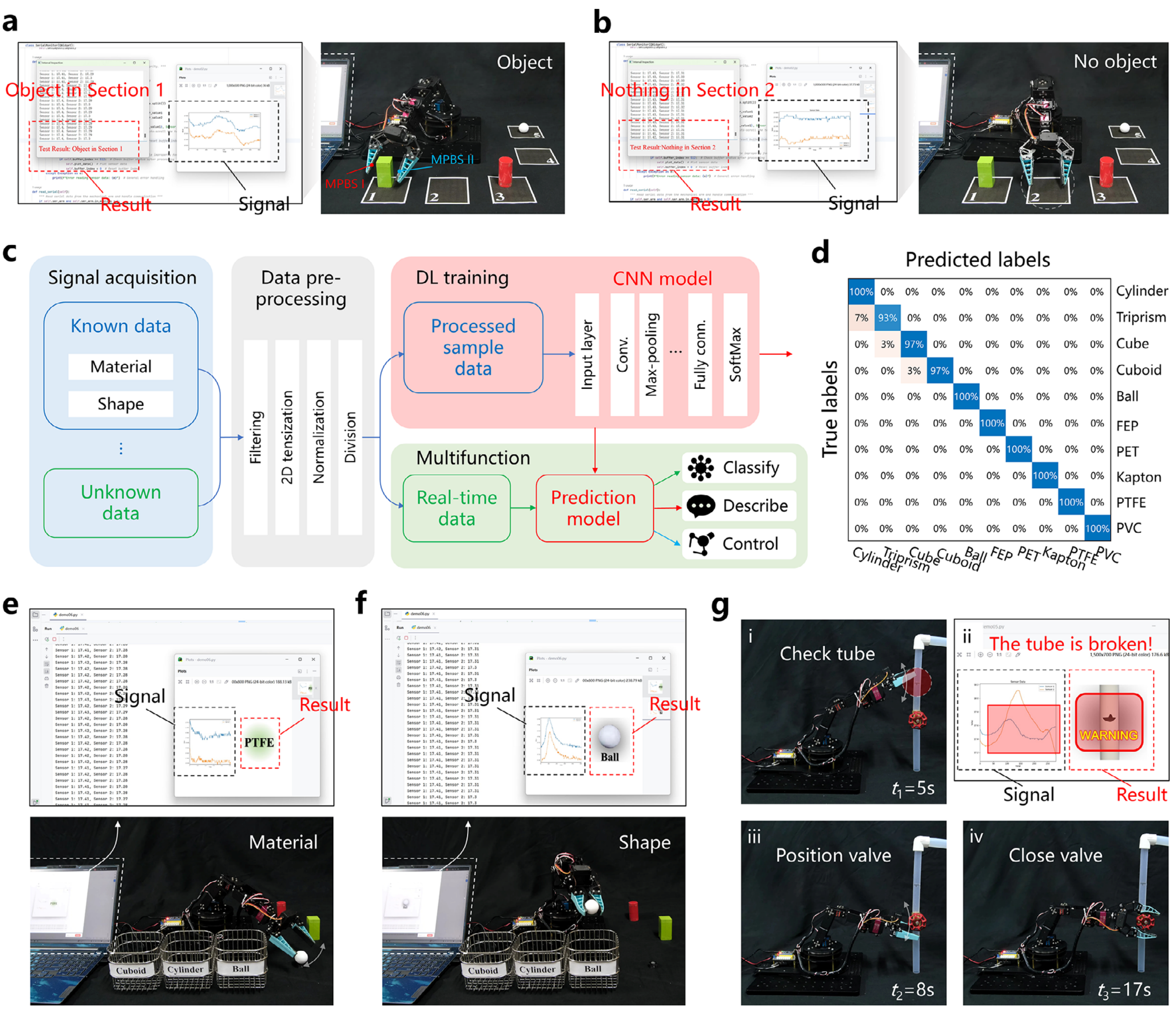

True labels \ Predicted labels	Cylinder	Triprism	Cube	Cuboid	Ball	FEP	PET	Kapton	PTFE	PVC
Cylinder	100%	0%	0%	0%	0%	0%	0%	0%	0%	0%
Triprism	7%	93%	0%	0%	0%	0%	0%	0%	0%	0%
Cube	0%	3%	97%	0%	0%	0%	0%	0%	0%	0%
Cuboid	0%	0%	3%	97%	0%	0%	0%	0%	0%	0%
Ball	0%	0%	0%	0%	100%	0%	0%	0%	0%	0%
FEP	0%	0%	0%	0%	0%	100%	0%	0%	0%	0%
PET	0%	0%	0%	0%	0%	0%	100%	0%	0%	0%
Kapton	0%	0%	0%	0%	0%	0%	0%	100%	0%	0%
PTFE	0%	0%	0%	0%	0%	0%	0%	0%	100%	0%
PVC	0%	0%	0%	0%	0%	0%	0%	0%	0%	100%

Figure 6. Demonstration of potential applications for the integrated intelligent robotic arm system. Patrol mission for the robotic arm system: area where a) object exists or b) doesn't. c) Flow diagram of the intelligent robotic arm system for perceiving, describing, and sorting objects. d) Confusion map of the system recognizing mixed information about objects. Total accuracy: 98.7%. Query e) material and f) shape of the object successively in intelligent sorting. g) Detecting pipeline breakage by touchless signals and treating.

noncontact scanning over the object to obtain the output signals from the MPBSs and confirm its presence. ii) Inputting the signals to the CNN model, the robotic arm system first predicts and describes the object's material and displays on the screen. iii) After querying its material, the system responds by driving the arm segments and gripper to grasp the test object. iv) The soft finger deforms to perceive the shape, as shown in Figure 6f, and the real-time acquired signals are displayed on the screen, along with the corresponding description result 'Ball' and picture of the tested object. v) According to the predicted shape, the system guides the robotic arm to place the ball into the designated basket. To avoid interference, only one sensing mode is activated at a time. The switching between touchless and tactile modes is triggered by state updates of the robotic arm during task execution. The detailed switching mechanism is provided in Note S2 (Supporting Information). These scenarios demonstrate the practicability of the intelligent robotic arm system via MPBS and CNN in perceiving, describing, and classifying objects through the triboelectrification influenced by their physical properties.

Finally, we demonstrate that the integrated robotic arm system can conduct a pipeline inspection in touchless mode, successfully identifying and treating the pipeline breakage (Figure 6g; Movie S7 and S8 (Supporting Information)). When inspecting a pipeline with a length of 50 cm, the robotic arm sweeps the straight pipe section and the pipe section containing a valve in a segmented sequence, updating the state information of each section in real time on the system, as shown in Movie S7 (Supporting Information). As shot in Figure 6g,i), when the pipeline breakage is detected with the gripper scanning past, the system immediately reports the abnormal result for this section and displays the real-time touchless signals from two channels. Since the pipeline breakage port faces the MPBS I, a 'depression' is formed at the generated signal peak, as shown in ii), which is due to the destruction of the continuous and uniform electric field caused by the defect.[35] In contrast, the MPBS II shows a complete and significant waveform peak. The waveform depression, as a key feature, is employed here to locate and identify the pipeline breakage. In the subsequent scanning iii), the system identifies and confirms the position of the valve. (iv) According to the programmed commands, the robotic arm is directed to perform the operation of closing the valve with the gripper after the system receives the alarm. The entire process flow of anomaly detection and emergency response takes ≈20 s. The experimental results indicate that, with an actual pipeline as the target, the developed MPBS and touchless-tactile control framework have endowed the robotic arm with excellent perception and execution capabilities, for which the application scenarios and potentials are further expanded and explored.

Despite our advances in new sensor design and its integration in robot hands (described in Figure 2 and 4), the development of new techniques to process and interpret the data they provide, and the demonstration of the potential applications (described in Figure 6), there are undeniably several limitations in the current system.

1) The above demonstrations are conducted in a dry room temperature environment. The touchless sensing performance of the MPBS will be affected by rapid changes in external environmental temperature or humidity, since the increase in temperature or moisture encourages the trapped charge to escape from the shallow layer. Advanced surface coating strategies need to be explored in future work to effectively suppress environment-induced charge dissipation while preserving sensing sensitivity.

2) Increasing the number of MPBSs in the system and considering the structure of dexterous hands would enable the detection of more grasp positions and pressure distributions to obtain comprehensive shape information. Meanwhile, the multimodal fusion with visual data can be used for more precise decoupling of the material and pressure information, and even the surface roughness or texture of objects.[6,36]

3) In this study, querying a number of physical properties of an external object, such as shape and material, helps the robot to reason about unknown objects. Yet, our supervised learning model is unable to accurately describe unfamiliar objects. Apart from following the strategy proposed by Kong et al., which enriches the collected training data with generated pseudo-data to enhance the generalization ability of neural networks.[37] We are exploring the integration of Large Language Models into the system to continuously enhance its generalization performance and intelligence level.

4) Most of the study on force control with dexterous hands is aimed at controlling both grasping force and slippage to achieve a stable grasp. Benefiting from the triboelectrification, the triboelectric tactile sensor is especially adept at sensing the sliding signals during lifting and clamping. Future work should focus on the investigation of using model-based grasp planning, as well as triboelectric slip detection and force control, to solve the grasping and stable grasping problems of dexterous robot hands and allow the robot to operate in the real world with a high tolerance.

3. Conclusion

In summary, a self-driven MXene and PAN-based carbon fiber enhanced bimodal triboelectric sensor is developed to capture continuous motion and tactile information for robotic arms. The functional layer doped with MXene nanosheets and the electrode composed of PAN-based carbon fibers provide the MPBS with enhanced touchless sensing and tactile perception performance. When the doping weight ratio of MXene reaches 2 wt.%, the electrical outputs, including both V_{OC} and Q_{SC}, significantly double to 22.81 V and 6.58 nC, respectively. The touchless sensing capability of the optimized MPBS reaches 3.65 V cm cm^{-2} and 200 cm, which is the highest to our best knowledge among the previously reported touch-free sensors based on the triboelectric effect. By integrating MPBSs into soft fingers, this study realizes a soft gripper at the end of a commercial robotic arm with bimodal perception capabilities. The touchless signals provide valuable insights into object materials while the tactile mode enables precise perception of object shapes. Through the touchless sensing mode, the integrated robotic arm can autonomously explore objects and run control actions when unexpected events occur. A CNN model is employed to fuse the touchless and tactile information collected during the soft gripper manipulation, resulting in an intelligent robotic arm system that precisely perceives, stably grasps, and accurately describes objects' material and shape with an accuracy of 98.7%. The system, through the proposed bimodal perception and control framework, demonstrates reliability in complete specialized tasks including noncontact object detection, AI-assisted sorting, and autonomous pipeline inspection and emergency handling. The bionic MPBS provides direct and understandable signal mapping and feedback, facilitating simple and friendly programming and control based on bimodal signals, both of which not only enable our robotic arm's excellent perception and execution capabilities but also contribute to expanding new scenarios of human-robot interaction and robot use.

4. Experimental Section

Fabrication of the MPBS: The addition-cure silicone rubber compounds were selected from Ecoflex^{TM} 00–30 of Smooth-On Inc., which remained a stable liquid at room temperature. The MXene material was the multi-layered clay $Ti_3C_2T_x$ powder, purchased from Foshan Xinxi Technology Co. Ltd. The PAN-based carbon fiber felt was sourced from Tianjin Carbon Factory. The MXene nanosheets were fully ground using a mortar and pestle and weighed according to the desired doping weight ratio. The silicone rubbers were mixed 1A: 1B by weight, and the ground powder was added to the liquid mixture and stirred evenly. After vacuum degassing, the silicone rubber@MXene mixture was prepared for the following process. The carbon felt (W × L × THK: 1.4 cm × 6 cm × 2 mm) was attached to the bottom of a rectangular mold (W × L × H: 1.4 cm × 6 cm × 5 mm) made by 3D printing. Then, the above prepared liquid mixture was slowly poured onto the top surface of the carbon felt and tightly covered with sandpaper (100 meshes per unit area). Finally, the mixture was cured in a drying oven at 113 °F/45 °C for 1 h, and the dried MPBS was stripped from the mold and sandpaper. After demolding the MPBS, its surface was thoroughly rinsed with anhydrous ethanol and subsequently dried in a clean environment to prevent any residue or contamination.

Fabrication of the Soft Robotic Gripper: The FRE soft fingers were purchased from Shenzhen Youyeetoo Technology Co. Ltd., and its detailed drawing could be found in Figure S6 (Supporting Information). A Kapton film (with a thickness of 0.1 mm) was pasted on the electrode surface of the MPBS as an insulating layer. Then the insulating surface was attached to the finger surface with a thin layer of pure silicone rubber (Ecoflex$^{\mathrm{TM}}$ 00–30, Smooth-On Inc.) and cured at 104 °F/40 °C for 2 h. Two soft fingers thus manufactured are fastened by screws to a rigid gripper matching a commercial robotic arm (Km1, Hangzhou Yeahbot Technology Co. Ltd.).

Measurement of the MPBS: The surface morphologies of MXene nanosheets and PAN-based carbon fibers were characterized by the FE-SEM (TESCAN MIRA 4, TESCAN Ltd.). The linear motor (R-LP4, Dreamer Lab) equipped with a force transducer was used to simulate mensurable motions. The MPBS and its insulating support were fixed on a flat plate containing the linear motor. The external object was attached to the force transducer mounted on the actuator of the linear motor, which can cyclically approach or even press the MPBS while the motor operates. The fundamental characterizations of the materials were conducted using a universal testing machine (SARTEC SS-8600-1KN, SARTECTEST Ltd.). The tensile test specimens were prepared in a dumbbell shape according to the GB/T145-2001 standard, which is equivalent to ISO 37 for the tensile testing of rubber materials. The tests were carried out at room temperature with a loading rate of 100 mm/min until failure. The stress-strain response was recorded to determine the fracture strain. Cyclic tensile and compression tests were also performed to assess the mechanical stability under repeated loading. In the cyclic tensile mode, the specimens underwent 100 loading-unloading cycles with a maximum strain of 100%. For cyclic compression, cylindrical specimens were tested at a constant strain rate of 10 mm/min with a maximum strain of 50%. Due to the limitations of the testing machine, the number of cycles was limited to 100 for each test. The triboelectric signals of the MPBS prototype were measured by an electrometer (Keithley 6514, Tektronix Inc.) with a sampling frequency of 500 Hz. Integrated with the robotic gripper, all the signal acquisitions were switched to Arduino Uno R3 microcontrollers for further design.

Finite Element Analysis: A 3D model of the MPBS was constructed in the COMSOL Multiphysics software, where the Solid Mechanics Module in the Stationary was employed to analyze the strain and stress distribution of the sensor under an external force of 20 N. The sensor material was represented by silicone rubber, while external objects were modeled as wood. In this case, the key properties of materials included density, Young's modulus, and Poisson's ratio, with their exact values obtained from reliable online sources.

Training of the CNN model: The neural networks were developed in Python and trained on an ordinary performance computer (CPU: i5-12400F, Intel; GPU: GeForce GTX 1650, NVIDIA). The proposed CNN architecture consisted of three convolutional layers, three max-pooling layers, one adaptive average pooling layer, and one fully connected layer. The input dataset was randomly shuffled and split into training, validation, and testing sets in a fixed ratio of 7:2:1. Three sequential 1D convolutional layers (kernel size = 3) with ReLU activation functions were employed to extract from the input signal sequences. Max pooling down-sampled the feature maps and reduced computational complexity. The adaptive average pooling layer was used to compress the feature dimensions, enabling the model to handle varying input lengths while maintaining key spatial characteristics. The fully connected layer was included to further transform the extracted features. A Softmax layer was used as the final output to perform multi-class classification across the predefined shape and material categories.

Statistical Analysis: Statistical analysis was performed using Origin 2019b software. For the quantitative results shown in Figure 3d,g,j, data were presented as mean ± SD. Each data point represents the average of a group of measurements, with a sample size of $n = 5$ per group.

Supporting Information

Supporting Information is available from the Wiley Online Library or from the author.

Acknowledgements

F.D., Q.P., and G.-A. Y. contributed equally to this work. This work was supported by the National Natural Science Foundation of China (Grant No. 52371345), and the China Postdoctoral Science Foundation (Grant No. 2024M750297).

Conflict of Interest

The authors declare no conflict of interest.

Data Availability Statement

The data that support the findings of this study are available from the corresponding author upon reasonable request.

Keywords

convolutional neural networks, flexible sensors, robotic arms, tactile perception, triboelectric nanogenerators

Received: March 16, 2025
Revised: June 5, 2025
Published online:

---

[1] P. Li, X. P. Liu, *J. Phys.: Conf. Ser.* **2019**, *1267*, 012036.
[2] Z. Kappassov, J. A. Corrales, V. Perdereau, *Robot. Auton. Syst.* **2015**, *74*, 195.
[3] Y. C. Tong, H. T. Liu, Z. T. Zhang, *IEEE-CAA J. Automatica Sin.* **2024**, *11*, 301.
[4] C. E. Wang, C. Liu, F. F. Shang, S. Y. Niu, L. A. Ke, N. Zhang, B. B. Ma, R. Z. Li, X. Sun, S. Zhang, *Biosens. Bioelectron.* **2023**, *220*, 114882.
[5] a) S. Pyo, J. Lee, K. Bae, S. Sim, J. Kim, *Adv. Mater.* **2021**, *33*, 26; b) Y. Z. Qiu, C. F. Yan, Y. Zhang, S. X. Yang, X. Yao, F. W. Ai, J. J. Zheng, S. W. Zhang, X. G. Yu, E. B. Dong, *Natl. Sci. Rev.* **2025**, *12*, 14; c) W. L. Xu, G. Y. Zhou, Y. Z. Zhou, Z. B. Zou, J. L. Wang, W. F. Wu, X. M. Li, *IEEE Trans. Instrum. Meas.* **2024**, *73*, 11.
[6] a) S. J. Li, H. X. Yu, G. P. Pan, H. Z. Tang, J. W. Zhang, L. Q. Ye, X. P. Zhang, W. B. Ding, *IEEE Trans. Robot.* **2024**, *40*, 4484; b) S. L. Mu, S. J. Li, H. F. Zhao, Z. H. Wang, X. Xiao, X. Xiao, Z. A. Lin, Z. W. Song, H. Z. Tang, Q. H. Xu, D. K. Wang, W. W. Lee, C. S. Wu, W. B. Ding, *Nano Energy* **2023**, *116*, 108790.
[7] a) H. Y. Zhang, H. Li, Y. Li, *Nano Lett.* **2024**, *24*, 4002; b) W. B. Liu, Y. N. Duo, J. Q. Liu, F. Y. Yuan, L. Li, L. C. Li, G. Wang, B. H. Chen, S. Q. Wang, H. Yang, Y. C. Liu, Y. R. Mo, Y. Wang, B. Fang, F. C. Sun, X. L. Ding, C. Zhang, L. Wen, *Nat. Commun.* **2022**, *13*, 14.
[8] A. Noor, M. Z. Sun, X. Y. Zhang, S. Li, F. Y. Dong, Z. Y. Wang, J. C. Si, Y. J. Zou, M. Y. Xu, *Mater. Today Phys.* **2024**, *46*, 18.
[9] W. B. Liu, Y. Duo, X. Y. Chen, B. H. Chen, T. Z. Bu, L. Li, J. X. Duan, Z. H. Zuo, Y. Wang, B. Fang, F. C. Sun, K. Xu, X. L. Ding, C. Zhang, L. Wen, *Adv. Funct. Mater.* **2023**, *33*, 10.
[10] H. Y. Luo, G. Y. Pang, K. C. Xu, Z. Q. Ye, H. Y. Yang, G. Yang, *Adv. Mater. Technol.* **2021**, *6*, 10.
[11] Y. Xiong, Y. Wang, J. Zhang, L. Zheng, Y. Liu, H. Jiao, J. Yang, Z. L. Wang, Q. Sun, *Device* **2024**, *2*, 100472.
[12] T. Jin, Z. D. Sun, L. Li, Q. Zhang, M. L. Zhu, Z. X. Zhang, G. J. Yuan, T. Chen, Y. Z. Tian, X. Y. Hou, C. Lee, *Nat. Commun.* **2020**, *11*, 12.
[13] Y. Y. Lu, D. P. Kong, G. Yang, R. H. Wang, G. Y. Pang, H. Y. Luo, H. Y. Yang, K. C. Xu, *Adv. Sci.* **2023**, *10*, 9.
[14] H. Scheich, G. Langner, C. Tidemann, R. B. Coles, A. Guppy, *Nature* **1986**, *319*, 401.
[15] D. L. Shen, T. L. Du, F. Y. Dong, H. Cai, A. Noor, X. N. Du, Y. J. Zou, C. Lee, M. Y. Xu, *Int. J. Extreme Manuf.* **2025**, *7*, 33.

[16] W. Cho, S. Kim, H. Lee, N. Han, H. Kim, M. Lee, T. H. Han, J. J. Wie, *Adv. Mater.* **2024**, *36*, 16.

[17] X. Xi, D. D. L. Chung, *Carbon* **2019**, *145*, 734.

[18] W. L. Zhang, Y. X. Lu, T. Liu, J. M. Zhao, Y. H. Liu, Q. Fu, J. L. Mo, C. C. Cai, S. X. Nie, *Small* **2022**, *18*, 9.

[19] C. Zhao, Z. Y. Wang, Y. W. Wang, Z. Qian, Z. Tan, Q. Y. Chen, X. X. Pan, M. Y. Xu, Y. C. Lai, *Adv. Funct. Mater.* **2023**, *33*, 12.

[20] S. B. Tu, Q. Jiang, X. X. Zhang, H. N. Alshareef, *ACS Nano* **2018**, *12*, 3369.

[21] X. Xi, D. D. L. Chung, *Carbon* **2019**, *145*, 452.

[22] a) S. Peng, Y. E. Feng, Y. Liu, M. Feng, Z. S. Wu, J. H. Cheng, Z. T. Zhang, Y. J. Liu, R. L. Shen, D. A. Wang, *Nano Energy* **2022**, *104*, 107899; b) G. Ye, Q. Wu, Y. Chen, X. Wang, Z. Xiang, J. Duan, Y. Wan, P. Yang, *Adv. Fiber Mater.* **2024**, *6*, 1874; c) J. M. Ma, J. Q. Zhu, P. Ma, Y. Jie, Z. L. Wang, X. Cao, *ACS Energy Lett.* **2020**, *5*, 3005; d) Y. H. Xi, J. Hua, Y. J. Shi, *Nano Energy* **2020**, *69*, 104390; e) Y. J. Tang, H. Zhou, X. P. Sun, N. H. Diao, J. B. Wang, B. S. Zhang, C. Qin, E. J. Liang, Y. C. Mao, *Adv. Funct. Mater.* **2020**, *30*, 9; f) F. Wang, Z. W. Ren, J. H. Nie, J. W. Tian, Y. F. Ding, X. Y. Chen, *Adv. Mater. Technol.* **2020**, *5*, 9.

[23] S. M. Niu, Y. Liu, S. H. Wang, L. Lin, Y. S. Zhou, Y. F. Hu, Z. L. Wang, *Adv. Funct. Mater.* **2014**, *24*, 3332.

[24] C. Xu, Y. L. Zi, A. C. Wang, H. Y. Zou, Y. J. Dai, X. He, P. H. Wang, Y. C. Wang, P. Z. Feng, D. W. Li, Z. L. Wang, *Adv. Mater.* **2018**, *30*, 9.

[25] H. Y. Zou, Y. Zhang, L. T. Guo, P. H. Wang, X. He, G. Z. Dai, H. W. Zheng, C. Y. Chen, A. C. Wang, C. Xu, Z. L. Wang, *Nat. Commun.* **2019**, *10*, 9.

[26] X. W. Shan, L. Birglen, *Int. J. Robot. Res.* **2020**, *39*, 1686.

[27] Q. F. Shi, Z. X. Zhang, T. Y. Y. He, Z. D. Sun, B. J. Wang, Y. Q. Feng, X. C. Shan, B. Salam, C. Lee, *Nat. Commun.* **2020**, *11*, 11.

[28] Y. Xiong, Y. Liu, J. H. Yang, Y. F. Wang, N. Xu, Z. L. Wang, Q. J. Sun, *Nano Energy* **2024**, *129*, 109956.

[29] Y. K. Zhou, M. L. Shen, X. Cui, Y. C. Shao, L. J. Li, Y. Zhang, *Nano Energy* **2021**, *84*, 105887.

[30] Z. X. Zhang, T. Y. Y. He, M. L. Zhu, Z. D. Sun, Q. F. Shi, J. X. Zhu, B. W. Dong, M. R. Yuce, C. K. Lee, *npj Flex. Electron.* **2020**, *4*, 12.

[31] a) G. Lee, J. H. Son, S. Lee, S. W. Kim, D. Kim, N. N. Nguyen, S. G. Lee, K. Cho, *Adv. Sci.* **2021**, *8*, 8; b) X. E. Guo, Z. D. Sun, Y. Zhu, C. K. Lee, *Adv. Mater.* **2024**, *36*, 16.

[32] H. B. Yan, M. H. Ang, A. N. Poo, *Int. J. Soc. Robot.* **2014**, *6*, 85.

[33] R. D. Howe, *Advanced Robotics* **1993**, *8*, 245.

[34] M. Prats, Á. P. d. Pobil, P. J. Sanz, *Robot Physical Interaction through the combination of Vision, Tactile and Force Feedback: Applications to Assistive Robotics*, Springer Publishing Company **2012**, https://doi.org/10.1007/978-3-642-33241-8.

[35] H. F. Zhao, H. Wang, H. Y. Yu, Q. H. Xu, X. S. Li, J. Guo, J. J. Shao, Z. L. Wang, M. Y. Xu, W. B. Ding, *Energy Environ. Sci.* **2024**, *17*, 2228.

[36] J. R. Yu, X. X. Yang, G. Y. Gao, Y. Xiong, Y. F. Wang, J. Han, Y. H. Chen, H. Zhang, Q. J. Sun, Z. L. Wang, *Sci. Adv.* **2021**, *7*, 9.

[37] D. P. Kong, G. Yang, G. Y. Pang, Z. Q. Ye, H. H. Lv, Z. W. Yu, F. Wang, X. V. Wang, K. C. Xu, H. Y. Yang, *Adv. Intell. Syst.* **2022**, *4*, 13.